Research Square

Preprints are preliminary reports that have not undergone peer review.
They should not be considered conclusive, used to inform clinical practice,
or referenced by the media as validated information.

Eliglustat-Induced Remodeling of Sulfo-Glycosphingolipid Metabolism and Gene Expression in hepatocellular carcinoma cells

Rachele Giannecchini
Fondazione IRCCS Istituto Nazionale dei Tumori
Matteo Niero
Fondazione IRCCS Istituto Nazionale dei Tumori
Fabio Bozzi
Fondazione IRCCS Istituto Nazionale dei Tumori
Federica Padelli
Fondazione IRCCS Istituto Nazionale dei Tumori
Alessia Bertolotti
Fondazione IRCCS Istituto Nazionale dei Tumori
Antonino Belfiore
Fondazione IRCCS Istituto Nazionale dei Tumori
Luca Agnelli
Fondazione IRCCS Istituto Nazionale dei Tumori
Silvia Ghislanzoni
Fondazione IRCCS Istituto Nazionale dei Tumori
Italia Bongarzone
italia.bongarzone@istitutotumori.mi.it

Fondazione IRCCS Istituto Nazionale dei Tumori

Article

Keywords: glycosphingolipid, lactosylceramide, hepatocellular carcinoma, MALDI mass spectrometry

Posted Date: August 12th, 2026

DOI: https://doi.org/10.21203/rs.3.rs-10534246/v1

License: This work is licensed under a Creative Commons Attribution 4.0 International License.
Read Full License

Additional Declarations: No competing interests reported.

Abstract

Dysregulation of glycosphingolipid (GSL) metabolism contributes to cancer progression by altering membrane organization, signaling pathways, and cellular adaptation. Sulfated glycosphingolipids (Sulfo-GSLs), including sulfated lactosylceramide, are elevated in several malignancies and have been implicated in tumor cell adhesion and metastasis. We previously identified elevated Sulfo-GSL levels in hepatocellular carcinoma (HCC) HepG2 cells, suggesting that targeting GSL biosynthesis may represent a potential therapeutic strategy. Here, we investigated the molecular consequences of UDP-glucose ceramide glucosyltransferase (UGCG) inhibition by eliglustat in HepG2 by integrating MALDI mass spectrometry-based lipid profiling with RNA sequencing. Eliglustat treatment induced dose-dependent remodeling of the cellular lipid profile, characterized by marked reduction of Sulfo-GSL species and a concomitant increase in selected phosphatidylinositol species. Lipidomic analysis revealed differential sensitivity of Sulfo-GSL molecular species, with preferential depletion of non-hydroxylated forms and relative preservation of hydroxylated species, indicating distinct metabolic responses within the same lipid class. Transcriptomic changes were limited at 20 μM eliglustat, whereas 30 μM induced extensive transcriptional reprogramming involving activation of immediate-early response genes, including EGR, FOS/JUN, and KLF family members, together with enrichment of inflammatory, stress-response, and senescence-associated pathways. Conversely, pathways related to cell-cycle progression, DNA replication, and chromatin organization were suppressed. Genes involved in GSL metabolism were also modulated, suggesting activation of compensatory mechanisms to restore lipid homeostasis. These findings demonstrate that UGCG inhibition induces coordinated lipidomic and transcriptional remodeling in HepG2, revealing both tumor-suppressive molecular features and adaptive responses to metabolic stress providing new insights into the cellular consequences of targeting GSL metabolism in HCC.

Introduction

Glycosphingolipids (GSL) are bioactive components of the plasma membrane that regulate key cellular processes, including signal transduction, cell-cell interactions, and membrane organization. Dysregulation of GSL metabolism is increasingly recognized as a hallmark of malignant transformation and tumor progression, influencing proliferation, survival, invasion, and therapeutic response in multiple solid tumors. Among GSLs, sulfate glycosphingolipids (Sulfo-GSL) constitute a distinct subclass generated by sulfation of GSL precursors. This group includes lactosylceramide sulfate and galactosylceramide sulfate, have emerged as important modulators of cancer cell behavior across multiple tumor types [1]. Elevated Sulfo-GSL levels have been reported in numerous human malignant tissues, including kidney, ovary, colon, stomach, and lung cancers [1–3]. Sulfo-GSL can enhance malignant phenotypes through interactions with growth factors and adhesion molecules. Furthermore, alterations in Sulfo-GSL composition have been shown to predict lymph node metastasis in colorectal cancer [4].

Using mass spectrometry (MS), we previously detected abundant expression of Sulfo-GSL in hepatocellular carcinoma (HCC) HepG2 cells [5]. In particular, we identified high levels of

lactosylsulfatide, also known as SM3 or Sulfo-dihexosylceramides/SulfoHex2Cer [6–8], one of the major GSL, which has been reported to play a role in cellular adhesion, an important step in tumor metastasis [9, 10]. Inhibition of Sulfo-GSL synthesis through iron depletion using deferoxamine induced apoptosis and, to a lesser extent, cellular senescence [5]. However, further investigation is required to clarify whether Sulfo-GSL represent a viable therapeutic target in HCC.

The first committed step of GSL biosynthesis is catalyzed by UDP-glucose: ceramide glucosyltransferase (UGCG), which converts ceramide into glucosylceramide (GlcCer), the metabolic precursor of lactosylceramide and Sulfo-GSL. Enhanced UGCG activity may contribute to the accumulation of downstream GSLs, including lactosylsulfatides. Under physiological conditions, GlcCer homeostasis is maintained through lysosomal degradation mediated by β-glucocerebrosidase. Therefore, deficiency of this enzyme in Gaucher disease leads to GlcCer accumulation and can be treated either by enzyme replacement therapy (ERT) or by substrate reduction therapy (SRT) [11], which inhibits UGCG using compounds such as miglustat, thereby reducing GlcCer synthesis.

Previous studies have reported that UGCG gene expression is altered in a low proportion of patients with HCC, a finding that has been implicated in the development of sorafenib resistance [11].

Jennemann *et al*.[12] demonstrated that treatment with the UGCG inhibitor Genz-123346 reduced tumor burden in a colorectal cancer mouse model. Mice receiving Genz-123346 showed fewer and smaller tumors together with reduced Ki67-positive cells in colon crypts, suggesting that UGCG inhibition may represent a novel therapeutic approach.

Eliglustat tartrate (Genz-112638), a more selective UGCG inhibitor, is approved for the treatment of Gaucher disease and has been evaluated in clinical studies for pediatric cancers [13, 14]. Eliglustat has been reported to enhance the growth-inhibitory effects of sorafenib and doxorubicin in both monolayer and spheroid HCC culture models [15]. Overall given that HCC patients frequently develop drug resistance to systemic therapies, and that sorafenib treatment is associated with increased UGCG expression, targeting GSL synthesis may represent a promising strategy to overcome therapeutic resistance [16, 17]. Recent studies have also highlighted a role for eliglustat in modulating antitumor immunity, extending its therapeutic relevance beyond direct effects on tumor cells. Notably, combining eliglustat with immune checkpoint blockade (ICB) was shown to induce robust $CD8^+$ T-cell responses and improve antitumor efficacy by inhibiting GSL synthesis across multiple tumor models [18]. Early proof-of-concept clinical studies suggest that this combination exhibits a favorable safety profile.

In this study, we hypothesized that the dependency of HepG2 cells on Sulfo-GSL metabolism represents a metabolic vulnerability that can be exploited by targeting GSL synthesis with eliglustat.

The aim was to investigate whether the reduction of Sulfo-GSLs induced by eliglustat is accompanied by a broad transcriptional reprogramming in HepG2 cells and whether this reprogramming is associated with the remodeling of signaling and metabolic pathways relevant to tumor cell behavior. Specifically, we

aimed to establish whether the molecular changes elicited by eliglustat preferentially reflect antitumor responses or, conversely, adaptive programs linked to chemoresistance.

Results

Eliglustat treatment induces remodeling of the lipid profile of HepG2 cells

To test whether eliglustat selectively alters the Sulfo-GSL lipid pool in HepG2 cells, we performed matrix-assisted laser desorption/ionization mass spectrometry (MALDI-MS) based lipidomic profiling following treatment with increasing concentrations of the drug (10, 20, and 30 μM). Within this class, SulfoHex2Cer corresponds to sulfated lactosylceramide, while SulfoHexNAcHex2Cer is generated by further glycosylation of SulfoHex2Cer within the same biosynthetic pathway (Fig. 1A). Eliglustat treatment induced clear changes in the relative peak intensities across the lipid spectra (Fig. 1B). Principal component analysis (PCA) was performed on MALDI-MS data acquired in negative ionization mode, and the resulting score plots revealed a separation between control and eliglustat-treated cells, consistent with the known effects of UGCG inhibition (Fig. 1C). This separation was particularly pronounced at the highest concentration tested (30 μM).

Although Sulfo-GSL species represented the primary focus of this study, alterations in additional lipid classes were also detected. At the highest dose tested, a slight decrease in phosphatidylethanolamine (PE) species with mass-to-charge (*m/z*) ratios between 700 and 800 was observed. Species-dependent changes were also detected in cardiolipin (CL) (*m/z* 1350–1500) and a modest increase in sphingomyelin (SM) (*m/z* 680–800). More pronounced alterations were detected in Sulfo-GSL species, which exhibited a substantial reduction in signal intensity across multiple species (*m/z* 900–1300) (heat map shown in Supplementary Fig. 1). Among the other lipid classes, phosphatidylinositol (PI) species (*m/z* 800–920), showed a marked increase (Fig. 1B). As illustrated in Fig. 1D, the intensity of PI(38:3) increased in a dose-dependent manner following eliglustat treatment. This trend suggests that the decrease in Sulfo-GSL levels is accompanied by a compensatory increase in PI species, with additional PI species displaying similar upregulation patterns.

Main peaks were annotated by tandem mass spectrometry (MS/MS) analysis the using the laser-induced fragmentation (LIFT) method and the LIPID MAPS structure database. PIs were identified based on diagnostic fragments at *m/z* 223, 241, and 259, with *m/z* 241 representing the dominant fragment. The most abundant PI species were PI 34:1, PI 36:1, PI 38:3 and PI 38:4. In eliglustat-treated cells, noticeable changes were observed in peak clusters at *m/z* 940.6, 968.6, 996.6, 1022.6, 1050.7 and 1066.7. In the CL region, additional differences were identified in the peak intensity profiles of the previously characterized clusters CL 64:X, CL 66:X, CL 68:X, and CL70:X [5], suggesting quantitative rather than qualitative changes in these lipid species.

Modulation of Sulfo-GSL by Eliglustat

Statistical analyses were performed by comparing spectra from control and eliglustat-treated samples using MetaboAnalyst 5.0. A heatmap of normalized data across 159 aligned *m/z* features revealed pronounced changes in peak intensities following treatment (Supplementary Fig. 1). As shown in Fig. 2A, the top 15 discriminant lipid peaks clearly separated eliglustat-treated samples, particularly at 30 μM, from HepG2 cells controls. Among these features, 13 out of 15 *m/z* signals that decreased upon treatment were assigned to SulfoHex2Cer species (Fig. 2A), which differ in the composition of their ceramide backbone (fatty acyl chain length, unsaturation and hydroxylation) while one feature corresponded to a ceramide that increased in intensity, consistent with accumulation of ceramide precursors following inhibition of UGCG. Several Sulfo-GSL species were characterized. MS/MS fragmentation of SulfoHex2Cer species (Supplementary Fig. 2) was characterized by diagnostic ions at *m/z* 97, 241, and 403, consistent with Sulfo-GSL fragments derived from sulfated lactosylceramide (LacCer, Hex2Cer; where Hex indicates glucose or galactose, not distinguishable by MS). Sulfation occurs at the C3 hydroxyl group of the hexose moiety. The ceramide species was identified by MALDI-MS/MS in negative-mode, where the precursor ion at *m/z* 653 (exact *m/z* 652.62) may correspond to the alpha-hydroxylated ceramide due to the diagnostic presence of the *m/z* 266 (exact *m/z* 266.25) sphingosine backbone fragment and the *m/z* 384 (exact *m/z* 384.38) hydroxylated acyl amide fragment (Supplementary Fig. 3). However, their structural assignment remains tentative, since negative-ion fragmentation of ceramides and sulfatides can involve complex dissociation mechanisms, including charge-directed pathways and rearrangement processes that may generate secondary product ions [19, 20].

Selective remodeling of hydroxylated and non-hydroxylated Sulfo-GSL species

MALDI–MSI provides a useful approach for analyzing the spatial distributions of SulfoHex2Cer species, including both hydroxylated and non-hydroxylated forms. Spectra from control and treated HepG2 cells were examined to identify and characterize the distributions of ten SulfoHex2Cer species. The analysis revealed an alternating pattern of non-hydroxylated and hydroxylated SulfoHex2Cer species. Peak intensities of hydroxylated SulfoHex2Cers decreased following eliglustat treatment, but to a lesser extent than non-hydroxylated species (Fig. 3). SulfoHex2Cer species contain structurally variable ceramide moieties, with fatty acid chains differing in length and degree of unsaturation. Hydroxylation at the α-2 position of the fatty acid was observed in approximately half of the SulfoHex2Cer population, which may confer a conformation less sensitive to UGCG inhibition. Importantly, lipid annotation indicated that SulfoHex2Cer biosynthesis was only partially inhibited, with significant reductions observed primarily in non-hydroxylated species. Variations in intensity were also observed for SulfoHex2Cer species, showing an alternating pattern between non-hydroxylated and hydroxylated forms: non-hydroxylated species (e.g., 40:1 and 42:2) decreased, whereas the corresponding hydroxylated species (40:1-OH and 42:2-OH) remained almost unchanged (Fig. 3). Overall, treatment

with 30 μM eliglustat induced extensive remodeling of lipid species. This effect was particularly evident in lipids downstream of its enzymatic target, UDP-glucose ceramide UGCG, such as Sulfo-GSLs, which exhibited a selective reduction in the intensity of non-hydroxylated species. These alterations were accompanied by a compensatory increase in PI species, highlighting a profound reorganization of lipid composition in HepG2 cells.

Eliglustat induces dose-dependent transcriptional reprogramming in HepG2 cells

To investigate how inhibition UGCG modifies the transcriptomic profile of HepG2 cells, RNA-seq analysis was performed following treatment with 20 or 30 μM Eliglustat. A clear dose-dependent effect was observed. Treatment with 20 μM altered the expression of 83 transcripts (66 up-regulated and 17 down-regulated), whereas 30 μM induced a much broader transcriptional response, with 580 up-regulated and 390 down-regulated genes (Fig. 4A and B, and Supplementary Tables 1 and 2). Most of the genes modulated at 20 μM (62/83, ~ 75%) were also regulated at 30 μM, indicating a shared core transcriptional response across doses (Fig. 4C and Supplementary Table 3). Within this shared gene set, the majority (57/62) were up-regulated and included IGFBP1 (the most up-regulated gene; fold change -FC- +7.07), CXCL8 (FC + 6.43), NCF2, TNFRSF9, and transcription factors of the EGR family (EGR1–3), as well as KLF4 and KLF5. Additional up-regulated genes included FOS, FOSB, FOSL1, FOSL2, JUN, JUNB, and JUND, consistent with activation of AP-1–related transcriptional programs (Supplementary Table 2). Genes involved in cytoskeletal and signaling regulation, such as DOCK11 and ARHGEF4, were also increased. No significant expression of FA2H, encoding the major fatty acid 2-hydroxylase, was detected in the RNA-seq dataset despite the identification of hydroxylated SulfoHex2Cer species by MALDI-MS/MS.

Taking into account the up-regulation of the EGR1, EGR2, and EGR3 transcription factors (TFs) observed after eliglustat treatment, a list of their putative target genes was obtained from the C3 regulatory target gene sets collection of the Molecular Signatures Database (MSigDB) (https://www.gsea-msigdb.org/gsea/msigdb/collections.jsp; Supplementary Table 4). Accordingly, 29 of the 970 DEGs were included in the EGR motif-based gene set and were therefore considered putative EGR target genes (Supplementary Table 5). These included transcription factors and genes involved in inflammatory signaling, such as RELB and TNFRSF12A, which were up-regulated together with KLF4 and KLF5 (Fig. 4D).

Genes involved in ceramide and sphingolipid metabolism were significantly modulated at 30 μM, including up-regulation of sphingomyelin synthase 2 (SGMS2; FC + 3.07), UGCG (FC + 1.9), and down-regulation of N-acylsphingosine amidohydrolase 2 (ASAH2; FC − 1.89) and serine palmytoil transferase long chain base subunit 3 (SPTLC3; FC − 1.86), indicating coordinated regulation of ceramide metabolism pathways (Fig. 4E). Notably, SGMS2 up-regulation was consistent with the increased abundance of SM species detected by MALDI-MS (Fig. 1B), whereas ceramide accumulation following

UGCG inhibition was also observed in the lipidomic analysis (Fig. 2A), supporting a coordinated metabolic adaptation to altered ceramide homeostasis.

Ingenuity pathway analysis (IPA) showed enrichment of inflammatory and stress-related signaling pathways, including IL-6/JAK, IL-17, NF-κB, HMGB1, cGAS–STING, NAFLD, fibrosis, and senescence-associated pathways. In contrast, pathways related to cell cycle progression, DNA replication, DNA repair, and chromatin organization were significantly down-regulated (Fig. 5). Overall, Eliglustat treatment induced a dose-dependent transcriptional reprogramming characterized by activation of immediate early genes (EGR, FOS/JUN, KLF families), inflammatory signaling modules, and modulation of sphingolipid metabolism, together with suppression of proliferative and DNA maintenance pathways.

Discussion

In this study, we show that inhibition of UGCG by eliglustat induces a coordinated and dose-dependent reprogramming of both the transcriptome and lipidome in HepG2 cells. The transcriptional response is minimal at 20 μM and becomes markedly broader at 30 μM, indicating a threshold-dependent activation of a global cellular program. A key feature of the response is the rapid induction of immediate early genes, including members of the EGR, FOS/JUN, and KLF families, consistent with a primary stress-response and survival pathway transcriptional programs [21]. The concomitant up-regulation of inflammatory mediators such as CXCL8, TNFRSF9, and RELB supports activation of AP-1 and non-canonical NF-κB signaling pathways, suggesting that UGCG inhibition is sensed as a strong perturbation of cellular homeostasis. The enrichment of EGR-binding motifs further indicates that part of this transcriptional program may be directly coordinated through EGR-dependent regulatory networks. In HCC, EGR1 is generally considered a tumor suppressor, promoting apoptosis of liver cancer cells while also contributing to the maintenance of hepatic metabolic homeostasis, modulation of inflammatory responses, and protection against liver injury [22]. Consistent with this, a comprehensive analysis of EGR family members (EGR1–4) in HCC carcinoma demonstrated that EGR genes are frequently dysregulated in HCC and are associated with tumor biological features and clinical outcome, supporting their relevance as regulatory components of HCC pathobiology [23]. Nevertheless, accumulating evidence has demonstrated the dual roles of the EGR family in tumor biology and elucidated its regulatory mechanisms in immunity, metabolism, and cellular differentiation [24, 25]. The coordinated transcriptional response involving SGMS2, UGCG, ASAH2, and SPTLC3 suggests that HepG2 cells actively reprogram multiple nodes of the sphingolipid network to counterbalance the metabolic consequences of UGCG inhibition. Notably, the increased expression of SGMS2 was accompanied by an increase in SM species detected by MALDI-MS, whereas ceramide accumulation was also observed following eliglustat treatment. Together, these findings indicate that excess ceramide is at least partially redirected toward SM synthesis rather than being completely removed from the cellular sphingolipid pool. In contrast, the down-regulation of ASAH2 argues against enhanced ceramide catabolism through the sphingosine pathway, suggesting that the adaptive response preferentially involves redistribution of ceramide into structural membrane lipids rather than its degradation. At the same time, altered expression of SPTLC3, a component of the serine palmitoyltransferase complex involved in de novo

sphingolipid synthesis, indicates broader regulation of sphingolipid flux rather than a selective response restricted to a single metabolic step. Together, these changes are consistent with an adaptive remodeling program aimed at restoring sphingolipid homeostasis following pharmacological disruption of GSL biosynthesis. The concomitant up-regulation of UGCG further supports activation of a compensatory feedback mechanism attempting to restore glycosphingolipid synthesis despite persistent pharmacological inhibition of the enzyme [26, 27].

A particularly relevant finding is the selective remodeling of sphingolipid species, which reveals a differential behavior between hydroxylated and non-hydroxylated forms. Across Sulfo-GSL and related species, non-hydroxylated lipids were consistently reduced, whereas hydroxylated species were preserved. This pattern suggests that hydroxylation confers a relative resistance to UGCG-dependent metabolic perturbation, pointing to a differential sensitivity of lipid subpopulations to pathway inhibition. A differential sensitivity of hydroxylated and non-hydroxylated GSL species to pathway inhibition has previously been described. Babcock et al. reported that 2-hydroxylated and non-hydroxylated galactosylceramide/sulfatide species display distinct responses to inhibition of GSL biosynthesis, suggesting that hydroxylation influences substrate handling and remodeling dynamics within the pathway [28]. Consistent with these observations, our data show a relative preservation of hydroxylated GSL species following UGCG inhibition, suggesting that hydroxylation may confer reduced susceptibility to acute metabolic perturbation. Beyond their differential metabolic regulation, hydroxylated GSL possess unique biophysical properties that promote tighter lipid packing, enhanced intermolecular interactions, and increased membrane order [29]. Therefore, the persistence of hydroxylated GSL species after pharmacological inhibition of UGCG may have functional consequences by inducing structurally ordered membrane domains despite reduced GSL biosynthesis. Rather than representing merely residual metabolic intermediates, hydroxylated GSL may constitute a structurally specialized lipid fraction that contributes to membrane organization and homeostasis under conditions of metabolic stress. An unexpected observation was the apparent absence of FA2H transcripts despite the identification of hydroxylated SulfoHex2Cer species by MALDI-MS/MS. Because FA2H represents the major fatty acid 2-hydroxylase involved in the biosynthesis of α-hydroxylated sphingolipids, this discrepancy may reflect very low transcript abundance or alternative metabolic mechanisms. Further studies will be required to clarify the biosynthetic origin of these lipids.

Pathway analysis revealed activation of inflammatory and stress-associated signaling networks, including IL-6/JAK, NF-κB, cGAS–STING, and senescence-related pathways, together with suppression of cell cycle progression, DNA replication, and chromatin organization. This coordinated transcriptional signature is consistent with a transition from a proliferative state toward a stress-adapted, senescence-associated phenotype characterized by inflammatory signaling and functional alteration [30–32]. Importantly, lipidomic changes further reinforce this interpretation. The reduction of non-hydroxylated sulfatides suggests loss of highly organized membrane lipid domains associated with differentiation, whereas increased SMs and ceramides may enhance lipid raft formation and support sustained cytokine and stress signaling. Together, these changes indicate a transition toward a more dynamic and signaling-competent membrane architecture.

Overall, our data support a model in which UGCG inhibition triggers a coordinated transcriptional, metabolic, and lipidomic stress response. This response integrates inflammatory activation, metabolic adaptation, and membrane remodeling, while simultaneously suppressing proliferative programs. Within this framework, hydroxylated sphingolipids emerge as a potentially distinct functional pool, potentially contributing to membrane stability and representing a candidate mechanism of partial resistance or resilience in sphingolipid-targeted therapeutic contexts. In conclusion, perturbation of GSL metabolism extends beyond lipid depletion, driving a systems-level reprogramming of HCC cells that couples gene expression, immune signaling, and membrane lipid architecture.

Materials and methods

Chemicals and materials

All solvents (ULC-grade) were purchased from Merck (Italy) unless stated otherwise. 9-Aminoacridine (9AA) was purchased from Sigma-Aldrich (Italy). ITO glass slides were obtained from Bruker Daltonics GmbH (Bremen, Germany). Chloroform and ethanol (HPLC grade) were purchased from Sigma-Aldrich (Italy). Methanol (LC–MS grade) was purchased from Fisher Scientific (Italy).

Cell line and cultures

HepG2 cells were purchased from American Type Culture Collection (ATCC, Manassas, VA, USA; ATCC number: HB-8065) and maintained in Dulbecco's modified Eagle medium (DMEM; Gibco, Italy) supplemented with 10% fetal bovine serum (FBS; Gibco) at 37°C and 5% CO_2.

Treatments

Lipids from control and eliglustat-treated HepG2 cells were extracted using the Bligh and Dyer method [30]. Eliglustat (Merck) was dissolved in distilled water and added to the culture medium at final concentrations of 10, 20, or 30 μM. HepG2 cells were seeded at a density of 3×10^5 cells/mL, treated with eliglustat 24 h after plating, and incubated for an additional 48 h, as previously described by Ghislanzoni et al. [3].

Briefly, 300 μL of chloroform/methanol (2:1, v/v) was added to the cell pellet. The suspension was mixed at 1400 rpm for 15 min and sonicated for 4 min. Subsequently, 100 μL of deionized water was added to induce phase separation, and the suspension was mixed for 1 min before centrifugation at 3000 × g for 5 min at 20°C. The lower organic phase containing lipids was collected into a clean tube and dried using a SpeedVac concentrator. The dried lipid extract was resuspended in an appropriate volume of 2-propanol/acetonitrile (60:40, v/v) and sonicated. Finally, four 1-μL aliquots of each sample were spotted onto indium tin oxide-coated slides (ITO slides; Bruker Daltonics), dried in a desiccator for approximately 60 min, and stored at − 80°C until analysis.

Lipid extraction and MS analysis

Mass spectrometry imaging analyses were performed using an UltrafleXtreme MALDI-TOF mass spectrometer (Bruker Daltonics, Germany) operated in reflectron mode and equipped with a frequency-tripled 355 nm Nd:YAG laser with repetition rates of up to 10 kHz. Lipid extracts from control and eliglustat-treated HepG2 cells were spotted onto indium tin oxide (ITO)-coated slides as described above. Four 1-µL aliquots of each sample were deposited to generate an array of aligned spots. The array was coated with 9-aminoacridine (9-AA; Sigma-Aldrich), prepared at 10 mg/mL in 2-propanol/acetonitrile (60:40, v/v). Matrix application was performed using a TM-Sprayer nebulizer (HTX Technologies) with the nozzle temperature set to 80°C, a pressure of 10 psi, and a flow rate of 0.12 mL/min. After matrix deposition, the slides were kept in a desiccator until MALDI-MSI acquisition. Data were acquired in negative-ion mode under identical instrumental settings for all samples. Laser power and focus were manually optimized before each acquisition to ensure consistent signal intensity and spectral quality. Spectral acquisition was controlled using FlexImaging 4.1 (Bruker Daltonics) with a raster size of 20 µm. At each pixel, 200 laser shots were accumulated, and spectra were acquired at a digitizer sampling rate of 1.25 GS/s over an *m/z* range of 600–1600. Depending on the area covered by the lipid extract (approximately 5–7 mm²), 250–400 spectra were collected and averaged for each sample. Raw data from control and treated samples were co-registered, normalized to the total ion current (TIC), and visualized using FlexImaging. Data processing was performed with SCiLS Lab 2026 Pro (SCiLS GmbH). Datasets were imported, converted into the SCiLS SL format, normalized to TIC, and used to generate ion distribution maps together with box and dot plots of normalized peak intensities. Lipid identification was performed by MS/MS using LIFT approach described by Suckau et al. [31]. Characteristic product ions were matched with reference fragmentation patterns available in the LIPID MAPS Lipidomics Gateway. Because of the relatively low mass resolving power of the instrument (approximately 5000 at *m/z* 885.56), lipid assignments were considered accepted only when supported by both the MS/MS fragmentation pattern and previous reports in the literature. Peak intensity data were exported as CSV files and imported into MetaboAnalyst 5.0 for downstream statistical analyses, including volcano plot and heatmap generation. Prior to statistical analysis, data were normalized by sum, subjected to variance-stabilizing transformation, and autoscaled.

RNA extraction

RNA was extracted from untreated HepG2 cells and from HepG2 cells treated with Eliglustat (20 or 30 µM) for 72 h using the RNeasy Mini Kit (Qiagen, Santa Clarita, CA) on an automated QIAcube extractor (Qiagen, Santa Clarita, CA), following the manufacturer's instructions. The RNA quantity was measured using Qubit 4 (Agilent Technologies, Palo Alto, CA), and RNA integrity was assessed with the TapeStation 4200 (Agilent Technologies, Santa Clara, CA).

RNA-seq libraries

RNA-seq libraries were prepared using the Illumina Stranded Total RNA Prep, Ligation with Ribo-Zero™ Plus Kit (Illumina, San Diego, CA, USA; Cat. No. 20040525), according to the manufacturer's instructions.

Briefly, 100 ng of total RNA was used as input for library preparation. Ribosomal RNA (rRNA) was depleted prior to reverse transcription of the remaining RNA into cDNA. Sequencing libraries were then generated through adapter ligation followed by PCR amplification. Library concentration was quantified using a Qubit 4 Fluorometer, and library quality was assessed using the Agilent 4200 TapeStation System. Libraries were pooled at equimolar concentrations and diluted to a final concentration of 0.5 nM. Sequencing was performed on an Illumina NovaSeq 6000Dx platform (Illumina, San Diego, CA, USA) using a NovaSeq 6000 SP Reagent Kit v1.5 (200 cycles) to generate paired-end 2 × 75 bp reads. The raw FASTQ files have been deposited in the Gene Expression Omnibus (GEO) under accession number GSXXXXX. RNA-seq reads were aligned to the human reference genome (hg38) using the STAR aligner55, and gene-level read counts were generated using HTSeq-count. Gene expression analysis was performed using the Limma-Voom pipeline [x] implemented in R (version 4.4.2). Briefly, genes with low expression were filtered using the filterByExpr function from the edgeR package, and library sizes were normalized using the trimmed mean of M-values (TMM) method. Counts were then transformed to counts per million (CPM) and log2-transformed for downstream analyses. Differentially expressed genes (DEGs) between experimental groups were identified using the Limma-Voom pipeline, applying thresholds of false discovery rate (FDR) < 0.05 and absolute log2 fold change (|log2FC|) > 2.

EGR putative target analysis

Members of the EGR family possess highly conserved zinc finger DNA-binding domains that recognize GC-rich consensus sequences, typically represented by the motif GCG(G/T)GGGCG[18]A lists of putative EGR1 (269 genes), (EGR2 188 genes) and EGR3 (83 genes) target was obtained from the C3 regulatory target gene sets collection of the Molecular Signatures Database (MSigDB), which contains gene sets defined by the presence of conserved transcription factor binding motifs in gene promoter regions (Supplementary Table 4).

Ingenuity Pathway Analysis

To identify biological pathways associated with the selected feature genes, functional enrichment analysis was performed using Ingenuity Pathway Analysis (IPA, QIAGEN). Differentially expressed genes were uploaded into IPA and analyzed using the Core Analysis function. Canonical pathways were identified based on enrichment within the Ingenuity Knowledge Base, and statistical significance was assessed using a right-tailed Fisher's exact test. P-values were adjusted for multiple testing where applicable, and pathways were considered significantly enriched at p-value ≤ 2. Additionally, an absolute IPA z-score ≥ 3 were considered to predict pathway activation states, with positive and negative values indicating activation or inhibition, respectively.

Declarations

Availability of data materials

RNA Seq data were deposited into the Gene Expression Omnibus database under accession number: GSE342040 and are available at the following URL:https://www.ncbi.nlm.nih.gov/geo/query/acc.cgi?

acc=GSE342040

Conflits of interest

The authors declare no conflits of interest

Funding sources

This work received funding from the European Union's Horizon 2020 research and innovation programme under Grant Agreement No. 101016923 (101.13039/100010661) and was partially supported by the Italian Ministry of Health (Ricerca Corrente 2025).

Author contributions

Rachele Giannecchini: Data analysis, data curation, visualization, writing – review & editing.

Matteo Niero: Data analysis, data curation, visualization, writing – review & editing.

Fabio Bozzi: Conceptualization, data analysis, data curation, visualization, writing – review & editing.

Federica Padelli: Data acquisition, data analysis.

Alessia Bertolotti: Data acquisition, data analysis, writing – review & editing.

Antonino Belfiore: Data acquisition, data analysis, writing – review & editing.

Luca Agnelli: Data analysis, data curation, visualization, writing – review & editing.

Silvia Ghislanzoni: Conceptualization, study design, data acquisition, data analysis.

Italia Bongarzone: Conceptualization, study design, data analysis, data interpretation, writing – original draft, writing – review & editing, funding acquisition.

References

1. Takahashi, T. & Suzuki, T. Role of sulfatide in normal and pathological cells and tissues. *J. Lipid Res.* **53**, 1437–1450 (2012).
2. Zhuo, D., Li, X. & Guan, F. Biological Roles of Aberrantly Expressed Glycosphingolipids and Related Enzymes in Human Cancer Development and Progression. *Front. Physiol.* **9**, 466 (2018).
3. Sakakibara, N., Gasa, S., Kamio, K., Makita, A. & Koyanagi, T. Association of elevated sulfatides and sulfotransferase activities with human renal cell carcinoma. *Cancer Res.* **49**, 335–339 (1989).
4. Morichika, H., Hamanaka, Y., Tai, T. & Ishizuka, I. Sulfatides as a predictive factor of lymph node metastasis in patients with colorectal adenocarcinoma. *Cancer* **78**, 43–47 (1996).

5. Ghislanzoni, S. et al. Reduced sulfatide content in deferoxamine-induced senescent HepG2 cells. *International J. Biochem. Cell. Biology* **159**, (2023).
6. Hori, A. et al. Characterization of galactosyl and lactosyl sulfatide species in human serum by MALDI-TOF mass spectrometry. *Ann. Clin. Biochem.* **56**, 574–582 (2019).
7. Cheng, H., Sun, G., Yang, K., Gross, R. W. & Han, X. Selective desorption/ionization of sulfatides by MALDI-MS facilitated using 9-aminoacridine as matrix. *J. Lipid Res.* **51**, 1599–1609 (2010).
8. Jirásko, R. et al. MALDI Orbitrap Mass Spectrometry Profiling of Dysregulated Sulfoglycosphingolipids in Renal Cell Carcinoma Tissues. *J. Am. Soc. Mass. Spectrom.* **28**, 1562–1574 (2017).
9. Wu, X. Z., Honke, K., Zhang, Y. L., Zha, X. L. & Taniguchi, N. Lactosylsulfatide expression in hepatocellular carcinoma cells enhances cell adhesion to vitronectin and intrahepatic metastasis in nude mice. *Int. J. Cancer*. **110**, 504–510 (2004).
10. Wu, W. et al. Regulation of integrin αV subunit expression by sulfatide in hepatocellular carcinoma cells. *J. Lipid Res.* **54**, 936–952 (2013).
11. Byrne, F. L., Olzomer, E. M., Lolies, N., Hoehn, K. L. & Wegner, M. S. Update on Glycosphingolipids Abundance in Hepatocellular Carcinoma. *International Journal of Molecular Sciences* vol. 23 Preprint at (2022). https://doi.org/10.3390/ijms23094477
12. Jennemann, R. et al. Blockade of Glycosphingolipid Synthesis Inhibits Cell Cycle and Spheroid Growth of Colon Cancer Cells In Vitro and Experimental Colon Cancer Incidence In Vivo. *Int J. Mol. Sci* **22**, (2021).
13. Wingerter, A. et al. Exploiting Gangliosides for the Therapy of Ewing's Sarcoma and H3K27M-Mutant Diffuse Midline Glioma. *Cancers (Basel)*. **13**, 1–25 (2021).
14. Bennett, L. L. & Turcotte, K. Eliglustat tartrate for the treatment of adults with type 1 Gaucher disease. *Drug Des. Devel Ther.* **9**, 4639–4647 (2015).
15. Jennemann, R. et al. Glucosylceramide Synthase Inhibition in Combination with Aripiprazole Sensitizes Hepatocellular Cancer Cells to Sorafenib and Doxorubicin. *Int J. Mol. Sci* **26**, (2024).
16. Stefanovic, M. et al. Targeting glucosylceramide synthase upregulation reverts sorafenib resistance in experimental hepatocellular carcinoma. *Oncotarget* **7**, 8253–8267 (2016).
17. Tang, W. et al. The mechanisms of sorafenib resistance in hepatocellular carcinoma: theoretical basis and therapeutic aspects. *Signal Transduct. Target. Ther* **5**, (2020).
18. Dong, L. et al. Inhibition of glycosphingolipid synthesis with eliglustat in combination with immune checkpoint inhibitors in advanced cancers: preclinical evidence and phase I clinical trial. *Nature Communications 2024 15:1* 15, 6970- (2024).
19. Hsu, F. F., Turk, J., Stewart, M. E. & Downing, D. T. Structural studies on ceramides as lithiated adducts by low energy collisional-activated dissociation tandem mass spectrometry with electrospray ionization. *J. Am. Soc. Mass. Spectrom.* **13**, 680–695 (2002).

20. Hsu, F. F. & Turk, J. Studies on sulfatides by quadrupole ion-trap mass spectrometry with electrospray ionization: Structural characterization and the fragmentation processes that include an unusual internal galactose residue loss and the classical charge-remote fragmentation. *J. Am. Soc. Mass. Spectrom.* **15**, 536–546 (2004).
21. Llorens-Giralt, P. et al. Sequential activation of transcription factors promotes liver regeneration through specific and developmental enhancers. *Cell Genomics* **5**, (2025).
22. Wu, X. et al. Identification of EGR1 as a Key Diagnostic Biomarker in Metabolic Dysfunction-Associated Steatotic Liver Disease (MASLD) Through Machine Learning and Immune Analysis. *J. Inflamm. Res.* **18**, 1639 (2025).
23. Chen, R. et al. Engineering circular RNA for enhanced protein production. *Nat. Biotechnol.* **41**, 262–272 (2023).
24. Guo, R. et al. Multifaceted regulatory mechanisms of the EGR family in tumours and prospects for therapeutic applications (Review). *Int J. Mol. Med* **56**, (2025).
25. Hua, Y., Wang, H., Ye, Z., Zheng, D. & Zhang, X. An integrated pan-cancer analysis of identifying biomarkers about the EGR family genes in human carcinomas. *Comput Biol. Med* **148**, (2022).
26. Lingwood, C. A. Glycosphingolipid functions. *Cold Spring Harb Perspect. Biol.* **3**, 1–26 (2011).
27. Breslow, D. K. & Weissman, J. S. Membranes in Balance: Mechanisms of Sphingolipid Homeostasis. *Mol. Cell.* **40**, 267–279 (2010).
28. Babcock, M. C. et al. Substrate reduction therapy for Krabbe disease and metachromatic leukodystrophy using a novel ceramide galactosyltransferase inhibitor. *Sci Rep* **11**, (2021).
29. Eckhardt, M. & Fatty Acid 2-Hydroxylase and 2-Hydroxylated Sphingolipids: Metabolism and Function in Health and Diseases. *Int J. Mol. Sci* **24**, (2023).
30. Gorgoulis, V. et al. Cellular Senescence: Defining a Path Forward. *Cell* **179**, 813–827 (2019).
31. Kuilman, T., Michaloglou, C., Mooi, W. J. & Peeper, D. S. The essence of senescence. *Genes Dev.* **24**, 2463–2479 (2010).
32. Glück, S. et al. Innate immune sensing of cytosolic chromatin fragments through cGAS promotes senescence. *Nat. Cell. Biol.* **19**, 1061–1070 (2017).

Figures

Fig. 1 A,B,C,D

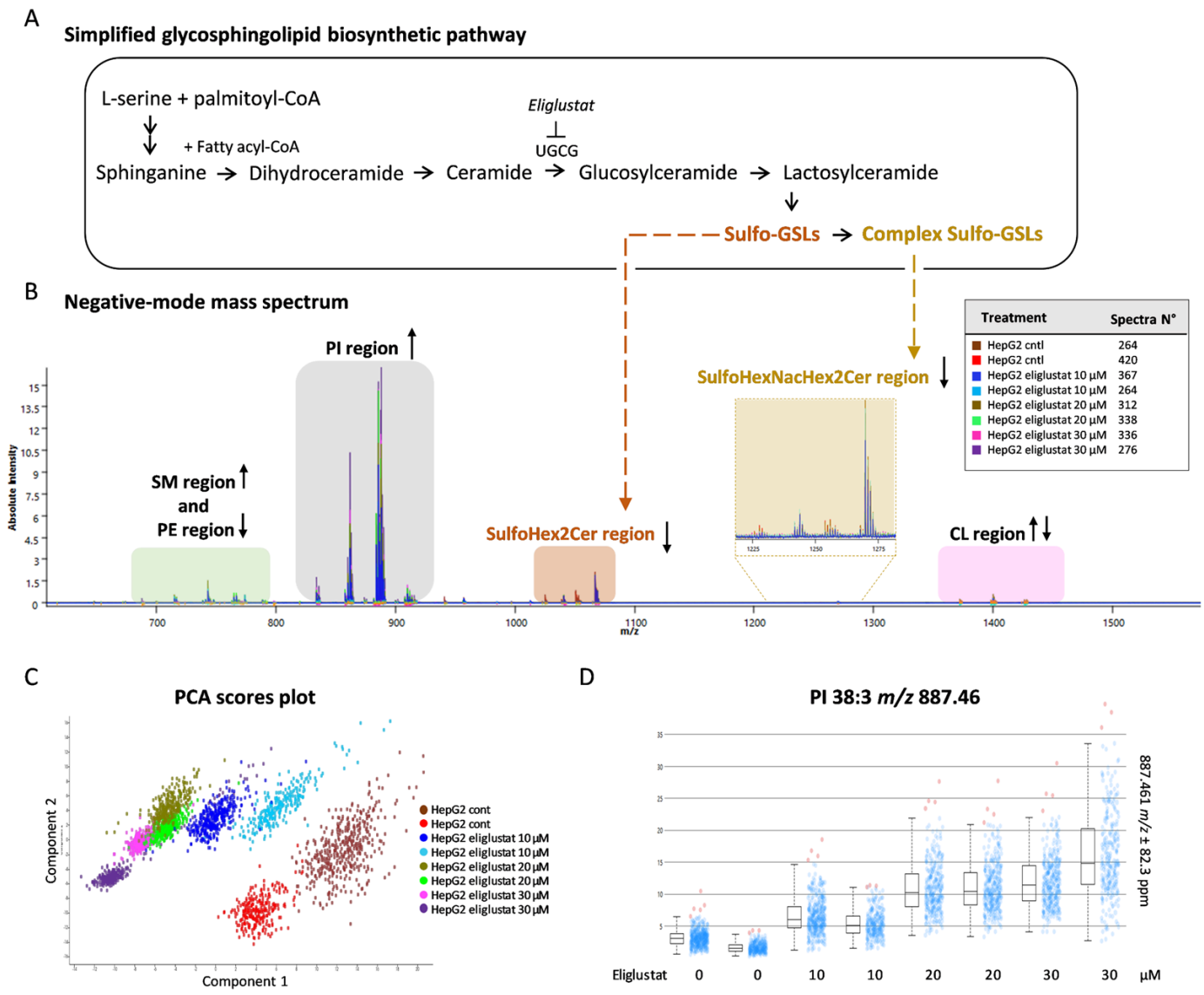


Figure 1

A. Simplified GSL biosynthetic pathway highlighting UGCG inhibition by eliglustat and the origin of the lipid classes detected by MALDI-MS. Ceramide, glucosylceramide, lactosylceramide and Sulfo-GSL, are represented as a pool of molecular species differing in acyl chain length, saturation and hydroxylation. **B**. Corresponding average negative-mode mass spectra of untreated and eliglustat-treated HepG2 cells. The major lipid regions are indicated. In both the SulfoHex2Cer and SulfoHexNacHex2Cer regions, peaks from untreated cells are consistently more intense than those from eliglustat treated cells, indicating depletion of sulfo-GSL species after UGCG inhibition. In contrast several peaks in the PI region increase in intensity with treatment **C**. PCA score plot obtained from 159 aligned peaks using principal components 1 and 2. **D**. Relative intensity variation of PI 38:3 at increasing eliglustat concentrations.

Fig. 2 A,B

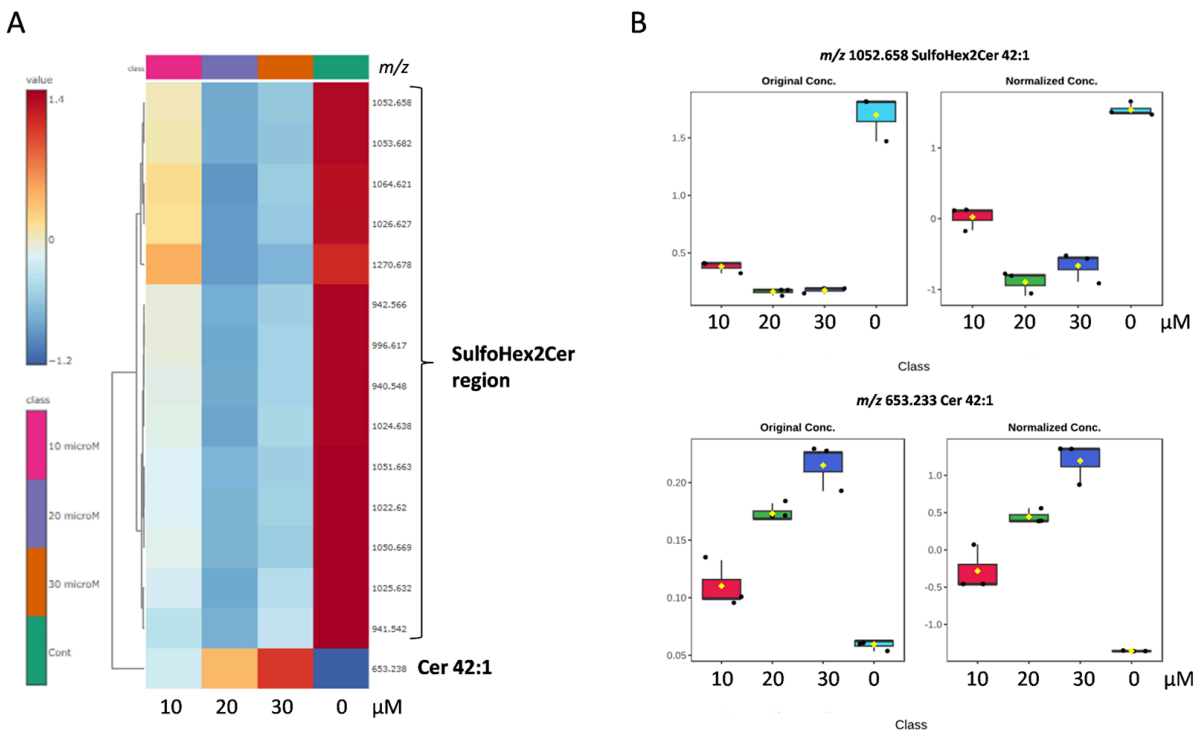


Figure 2

A. Heatmap generated using MetaboAnalyst 5.0 highlighting the eliglustat responses of SulfoHex2Cer species and Cer 42:1. B. Box plots depicting the expression of SulfoHex2Cer 42:2 and Cer 42:1 lipid species most strongly negatively or positively correlated with eliglustat treatments.

Fig. 3

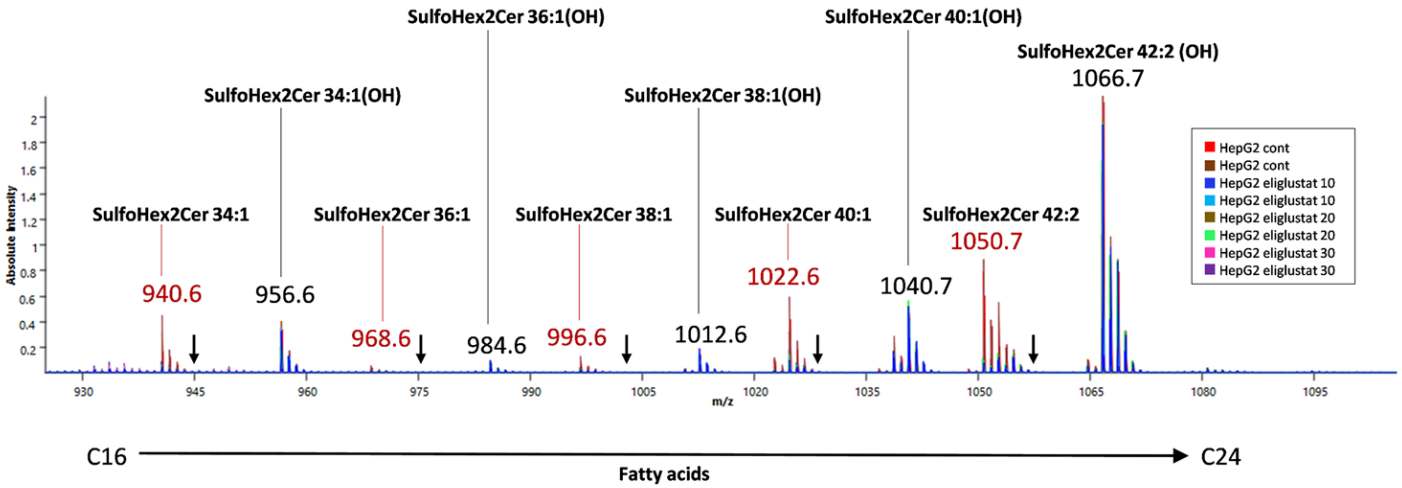


Figure 3

SulfoHex2Cer species spectral fingerprints of eliglustat-treated and untreated HepG2 cells.

Fig. 4 A,B,C,D,E

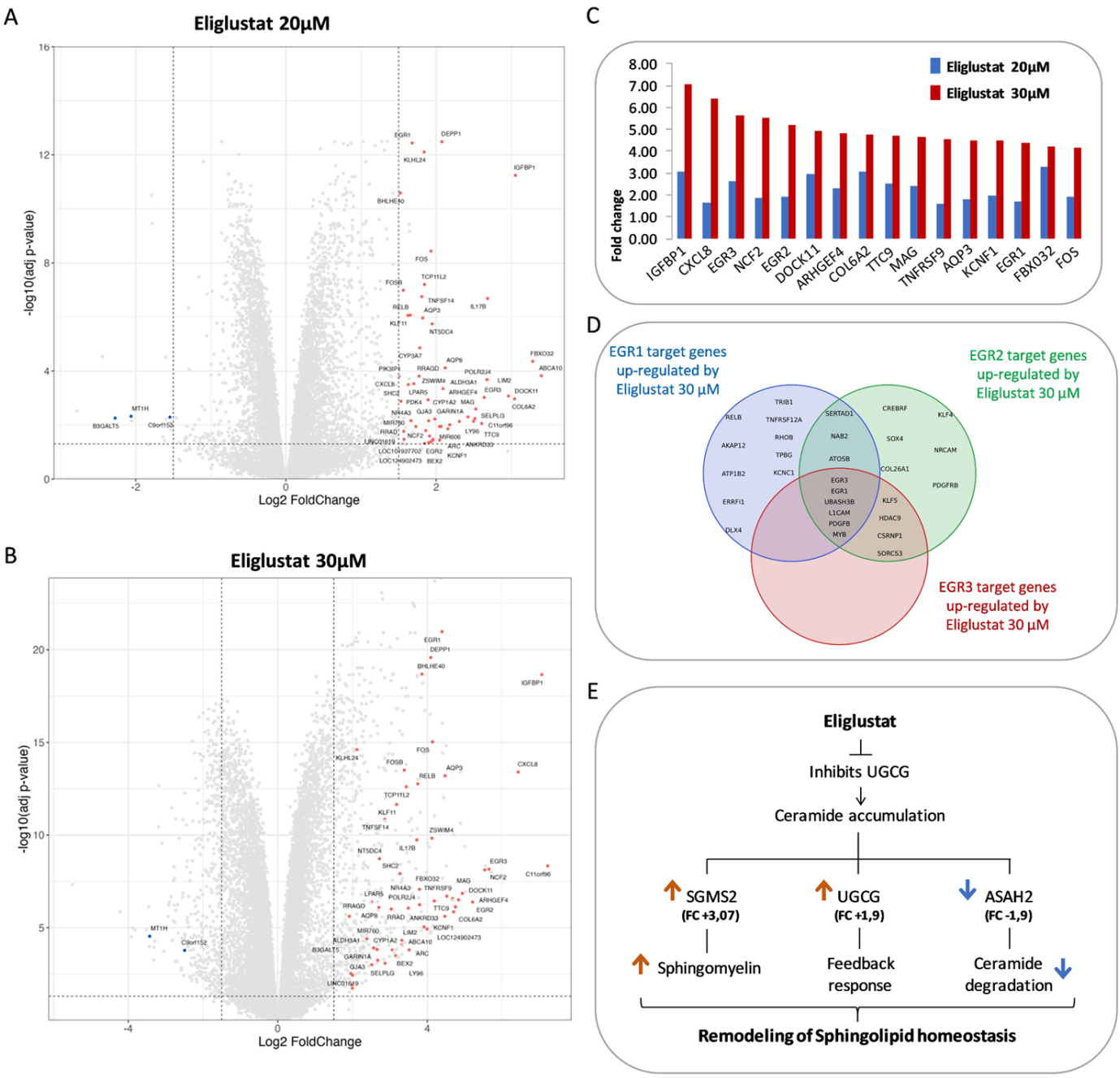


Figure 4

Transcriptomic response of HepG2 cells to Eliglustat treatment. Volcano plots showing differentially expressed genes (DEGs) following treatment with 20 µM (**A**) or 30 µM (**B**) Eliglustat. Up and down-regulated genes shared between treatments are highlighted in red and blue colors respectively. **C.** Bar plot showing the fold change of the top 16 transcripts upregulated at both drug concentrations. **D.**Venn diagram showing the differentially expressed transcription factors potentially regulated by the EGR family (EGR1, EGR2, and EGR3) following treatment with 30 µM Eliglustat. **4E.** Proposed model of sphingolipid remodeling induced by eliglustat in HepG2 cells.Pharmacological inhibition of UGCG by eliglustat results in ceramide accumulation, as detected by MALDI-MS, and is accompanied by

coordinated transcriptional changes involving SGMS2, UGCG, and ASAH2. The concomitant increase in sphingomyelin (SM) species and SGMS2 transcription suggests preferential redistribution of ceramide toward SM synthesis, whereas ASAH2 down-regulation is consistent with reduced ceramide catabolism through the sphingosine pathway. Together, these findings support a model in which HepG2 cells undergo adaptive remodeling of sphingolipid homeostasis in response to UGCG inhibition.

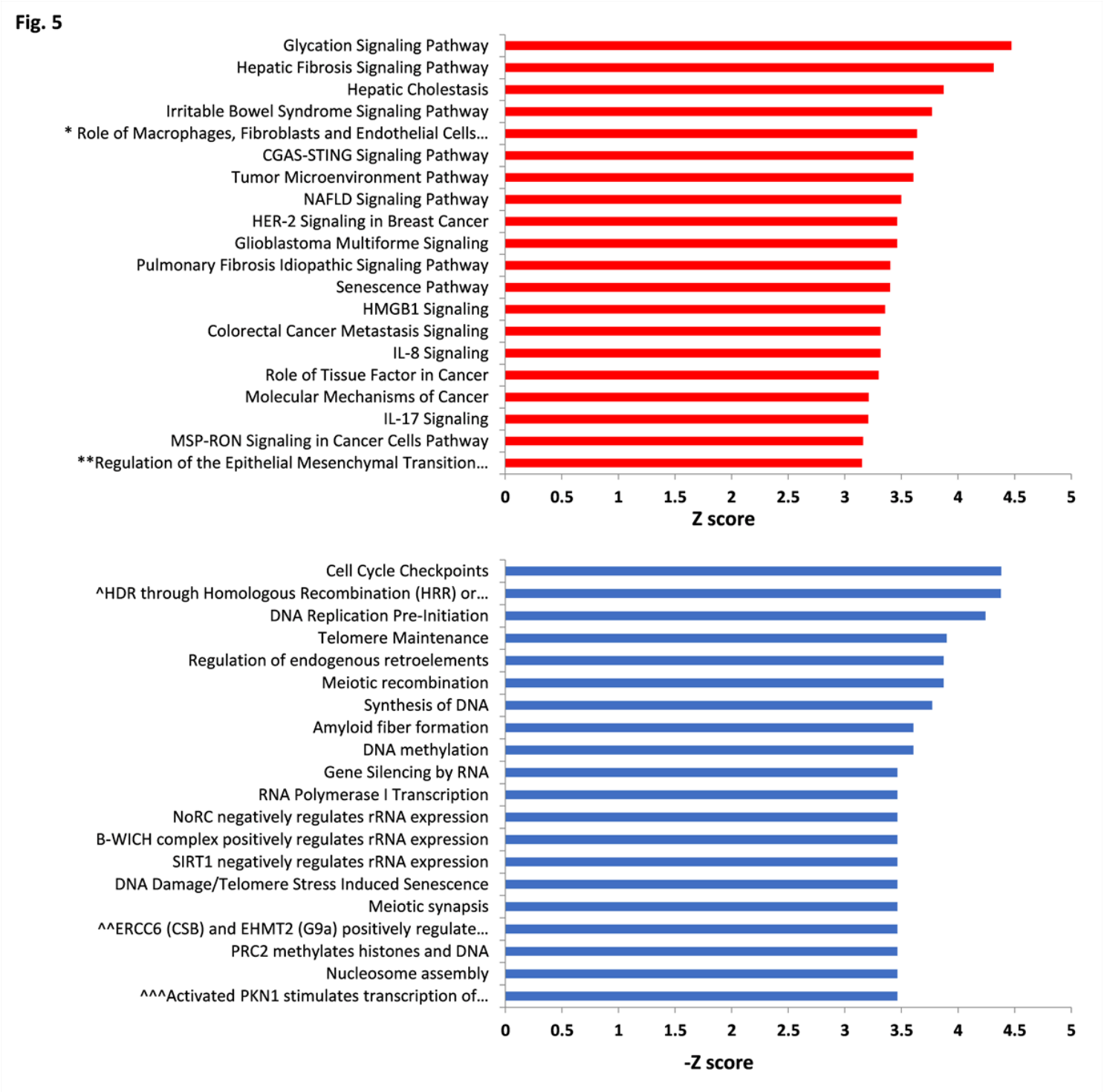


Figure 5

Ingenuity Pathway Analysis (IPA) of the 970 differentially expressed genes (DEGs). Pathways with an IPA activation z-score ≥ 3 were predicted to be activated (red bars), whereas those with a z-score ≤ −3 were predicted to be inhibited (blue bars).

*Role of Macrophages, Fibroblasts and Endothelial Cells in Rheumatoid Arthritis

**Regulation of the Epithelial Mesenchymal Transition by Growth Factors Pathway

^ HDR through Homologous Recombination (HRR) or Single Strand Annealing (SSA)

^^ERCC6 (CSB) and EHMT2 (G9a) positively regulate rRNA expression

^^^Activated PKN1 stimulates transcription of AR regulated genes KLK2 and KLK3

Supplementary Files

This is a list of supplementary files associated with this preprint. Click to download.

- Supplementaryfigures.pdf
- SupplementaryTable1.xlsx
- SupplementaryTable2.xlsx
- SupplementaryTable3.xlsx
- SupplementaryTable4.xlsx
- SupplementaryTable5.xlsx